Research Square

Preprints are preliminary reports that have not undergone peer review.
They should not be considered conclusive, used to inform clinical practice,
or referenced by the media as validated information.

Synthesis and visible-light photocatalytic degradation performance of BaNiO 3 /g-C 3 N 4 heterojunction for aniline blue degradation

Majed Al Harbi
Qassim University
Mohammed Alrashidi
Qassim University
Fehaid Alsubaie
King Abdulaziz City for Science and Technology
Abuzar Albadri
Qassim University
Abueliz Modwi
Qassim University
Fahad Alminderej
f.alminderej@qu.edu.sa
Qassim University
Mohamed Khitouni
Qassim University

Research Article

Keywords: Geen synthesis, Nanocomposite, Photodegradation, X-ray diffraction, Kinetics, Heterojunction

Posted Date: November 9th, 2026

DOI: https://doi.org/10.21203/rs.3.rs-11429076/v1

License: This work is licensed under a Creative Commons Attribution 4.0 International License.
Read Full License

Additional Declarations: No competing interests reported.

Synthesis and visible-light photocatalytic degradation performance of $BaNiO_3$/g-C_3N_4 heterojunction for aniline blue degradation

Majed S. Al Harbi[1], Mohammed A. Alrashidi[1], Fehaid Mohammed Alsubaie[2], Abuzar Albadri[1], Abueliz Modwi[1], Fahad Alminderej[1]*, Mohamed Khitouni[1]*

[1]Department of Chemistry, College of Science, Qassim University, Buraydah 51452, Saudi Arabia.
[2]Institute of Refining and Petrochemical Technologies, King Abdulaziz City for Science and Technology, P.O. Box 6086, Riyadh 11442, Saudi Arabia
*Correspondences: F.Alminderej@qu.edu.sa; Kh.mohamed@qu.edu.sa;

Abstract

A $BaNiO_3$/g-C_3N_4 heterojunction was synthesized via green synthesis approach using the *Peganum harmala* leaf extract as reducing agent. A comprehensive characterization of the pristine and nanocomposite photocatalysts was performed using XRD, FTIR, EDX, UV–vis DRS, and PL techniques to investigate their physicochemical properties. The microstructural data revealed the presence of $BaNiO_3$ and g-C_3N_4 phases with crystallite sizes ranging from approximately 10 to 60nm crystallite size and FTIR results confirmed the coexistence and interaction of characteristic functional groups associated with $BaNiO_3$ and g-C_3N_4. The UV–vis DRS analysis indicated a reduction of the $BaNiO_3$ bandgap energy from 3.31 to 2.86eV upon incorporation of g-C_3N_4, indicating improved visible-light absorption and optical response of heterojunction. The catalytic activity of developed composite was assessed through the degradation of the Aniline blue (AB) dye under visible light irradiation. The nanocomposite achieved 94% removal of AB dye within 80min, corresponding to a kinetic rate constant of 0.0273min^{-1}. Its enhanced photocatalytic performance is attributed associated with the formation of an intimate heterojunction between the two components, which can facilitate interfacial charge separation and suppress electron-hole recombination, as indicated by the PL results. Radical trapping experiments further revealed that $^{\bullet}OH$ and $^{\bullet}O^{2-}$ species play important roles in AB dye degradation.

Keywords: Geen synthesis; Nanocomposite; Photodegradation; X-ray diffraction; Kinetics; Heterojunction

1. Introduction

Industrial expansion is pervasively related to the dumping of large quantities of numerous toxic pollutants, which are detrimental to the environment, perilous to human and animal health, and difficult to destroy by simple natural routes [1-3]. Wastewater from industries such as paper and pulp, chemical, petrochemical, dyeing, etc. comprises injurious and persistent organic and inorganic contaminants which can cause harm to the environment [4-6]. Among the many

organic pollutants, dyes are the most commonly used types that are released to the aqueous environment [7-9]. They are hazardous, cancer-causing, toxic, and negatively impact human health, the atmosphere, and aquatic ecosystems. Organic molecules encompass aromatic rings, and particularly their nitro-, sulfo-, and chloro- series are generally present in manufacturing effluents and are the primary source of water pollution [10-12]. Humans' fascination for colored uniforms, colored foodstuff, and furniture has led to the indispensable use of colored dyes and pigments [13-15]. The color wastes from textile and color industries do not only cause the color problem in water bodies but also become a source of pollution for aquatic organisms by reducing or even blocking the light and interrupting the food chains and oxygen for aquatic life [16-18].

Aniline Blue (AB) is a triphenylmethane dye that includes three sulfonic acid groups, giving it acidic dye character, with λ_{max} = 597 nm. It is regularly used in the fabrics industry to shade a varied range of textiles [19, 20]. It is considered xenobiotic due to its discrete chemical structure, which makes it difficult to destroy [21]. AB is an extremely toxic dye and gives rise to coughing, breathing troubles, and gastric irritation, while, its long-term contact results in impairment of the blood's ability to transport oxygen [22, 23].

Several treatment procedures, including physical, chemical, and thermal decontamination approaches, have been followed to purify AB-adulterated wastewater. These outdated procedures have drawbacks such as low degradation efficacy, high energy usage, sludge generation, expensive and bulky equipment, and long residence time [24, 25]. The insufficiency of classical methods in dealing with these challenges made researchers adopt advanced oxidation processes (AOPs) [26-28]. These latter have gained significant attention for wastewater treatment due to their ability to generate highly reactive oxidizing species, particularly hydroxyl radicals (·OH). These processes include ozonation, Fenton and Fenton-like reactions, photocatalysis, electrochemical oxidation, and wet-air oxidation. The strong oxidation potential of ·OH (~2.8 V) enables the effective degradation of various organic pollutants. Use of $CoFe_2O_4$/g-C_3N_4/Bentonite, photo-Fenton in the presence of H_2O_2 involving the generation of reactive hydroxyl and perhydroxyl radicals for AB degradation [29]. The photodegradation of AB using banyan aerial root extract-derived silver nanoparticles was achieved with the assistance of the reducing agent $NaBH_4$ [21]. Of late, graphitic carbon nitride (g-C_3N_4) has attracted a lot of interest owing to its exceptional thermal and chemical stability. In contrast to conventional catalysts like TiO_2, which are restricted to the 5% UV region, it has a small bandgap (~ 2.7 eV) that enables it to absorb visible light, which makes up 45% of the solar spectrum [30, 31]. Furthermore, g-C_3N_4 is a cost-effective alternative to precious metal-based catalysts being formed of much abundant Earth element i.e. nitrogen and carbon

[31, 32]. Its special 2D layered assembly facilitates its binding to other metal and non-metal semiconductors. Despite its advantages, the practical application of g-C_3N_4 is hindered by the rapid recombination of photogenerated electron-hole pairs [33, 34]. Constructing a heterojunction by joining g-C_3N_4 with another material, like $BaNiO_3$, is expected to be an effective approach to get around this. By working as an "electron trap," this interface fruitfully diverts electrons away from the holes, extending the charge carriers' lifetime and empowering them to degrade organic dyes with strikingly higher efficiency [33, 35]. Because of its outstanding charge-transport capabilities and remarkable chemical and thermal stability, the perovskite $BaNiO_3$ was chosen with special consideration [36]. Charge carriers can flow more freely with less energy loss thanks to the synergy between $BaNiO_3$ and g-C_3N_4, which also increases the light-absorption range and lowers electron transfer resistance.

Methods such as sol-gel, metal nitrate decomposition, combustion, and molten salts were employed for obtaining $BaNiO_3$ nanoparticles [37, 38]. However, most of the synthesis protocols involve methods that are not economically feasible or environmentally friendly, and require multiple stages that generate undesirable by-products. To address these problems, an important step toward a sustainable route is the use of *Peganum harmala* extract in a green synthesis method. The bioactive ingredients found in *Peganum harmala* including alkaloids, flavonoids, triterpenoids, and anthraquinones [39, 40], serve as organic capping and reducing agents, covering the nanoparticles to keep them from aggregation and assuring a high specific area.

Without using expensive equipment or harmful precursors, this environmentally benign protocol permits the fabrication of high-performance catalysts under mild conditions. In this research, we report the effective fabrication of a novel $BaNiO_3$/g-C_3N_4 composite using a combination of sonochemical and mechanical methods. The leaf extract from *Peganum harmala* was used to manufacture the $BaNiO_3$ component. The prime goals of the study are to assess the composite's photocatalytic efficacy against Aniline Blue dye under visible light, describe its structural and optical characteristics, and clarify the fundamental mechanism of charge transfer and pollutant destruction.

2. Materials and Methods

2.1. Materials

All reagents were analytical grade and obtained from Sigma-Aldrich, including urea (≥99.5 %, pellets), barium nitrate [$Ba(NO_3)_2$], and nickel (II) nitrate hexahydrate [$Ba(NO_3)_2 \cdot 6H_2O$]. Fresh *Peganum harmala* leaves were collected from the Al-Qassim region.

2.2. Preparation of *Peganum harmala* Leaf Extract

Fresh leaves of *Peganum harmala* were hand-picked and dried, then using an Essa®LM2 pulverizing mill, the dry leaves were ground for one minute to get a homogenized powder of an average particle size less than 75 μm. About 30 g of the pulverized plant material was mixed with 300 mL of distilled water in a 400 mL beaker. The mixture was heated to 95 °C under continuous magnetic stirring at 800 rpm for 2 h to guarantee the maximal extraction of the bioactive ingredients. The obtained solution was allowed to cool naturally, and the extract was filtered using a vacuum filter to acquire a clear filtrate (Scheme 1).

2.3. Preparation of Graphitic carbon nitride (g-C_3N_4)

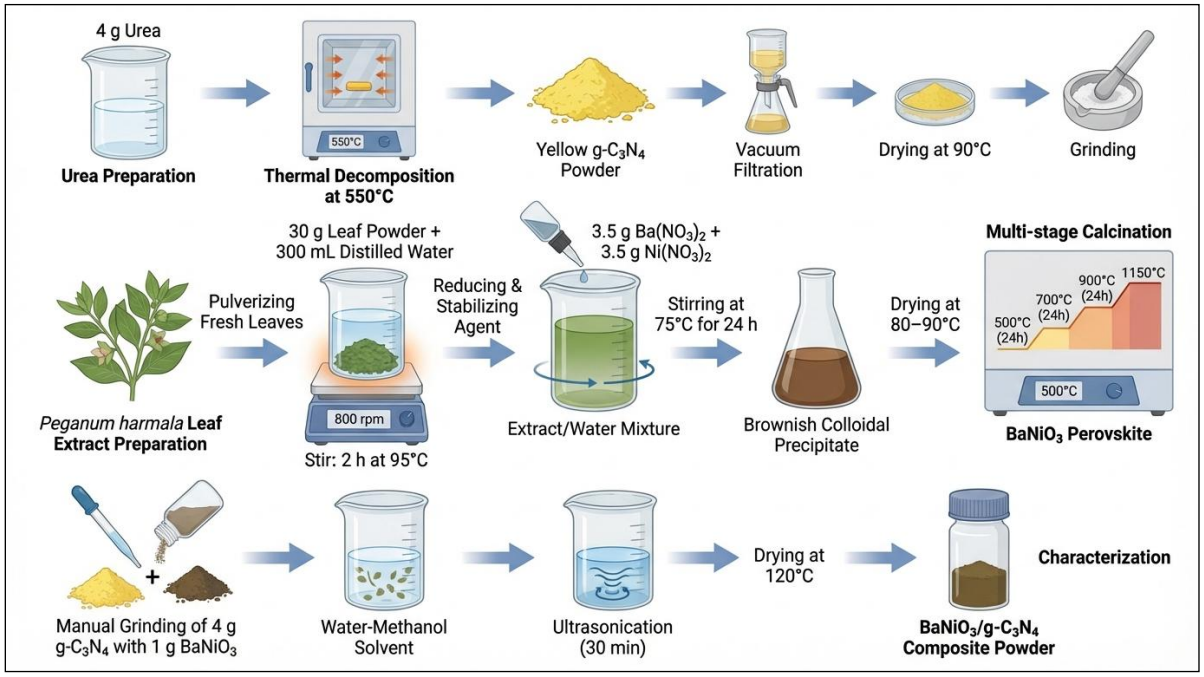
Graphitic carbon nitride (g-C_3N_4) was prepared by thermal decomposition of urea. Briefly, 4.0 g of urea was heated in a muffle furnace at 550°C for 2 h using a heating rate of 10°C/min in air. The resulting yellow solid was cooled to room temperature, vacuum-filtered, and dried at 90°C for 12 h. The resulting solid was gently pulverized to powder using a mortar and a pestle (Scheme 2).

2.4. Synthesis of $BaNiO_3$ Perovskite via Green Route

The perovskite $BaNiO_3$ was prepared adopting the green synthesis protocol, using the P. *harmala leaf* extract as a sustainable reducing and stabilizing agent. A precursor solution was made by dissolving 3.5 g of each of $Ba(NO_3)_2$ and $Ni(NO_3)_2$ in 100 mL total solution consisting of 1:1 plant extract-to-distilled-water ratio in a 150 mL beaker. The blend was heated at 75 °C under constant stirring at 800 rpm for 24 h. The lengthy duration was used to ensure that the bioactive components of the extract interacted with the metal ions. It led to the slow formation of a brownish colloidal precipitate, demonstrating the positive reduction of Ba^{2+} and Ni^{2+} ions and the start of $BaNiO_3$ nanoparticle formation. After the stirring process, the obtained suspension was poured into a glass dish and placed in a drying oven at 80–90 °C for 24 h. This step was performed to eliminate residual moisture and get a solid precursor. The dried mass was brown, to some extent cracked solid, signifying complete water evaporation and partial organic decomposition. Then, the dried precursor was subjected to multi-stage calcination to achieve complete crystallization of the $BaNiO_3$ perovskite phase. The sample was first calcined at 500 °C for 24 h, followed by grinding fine powder. The powder was then calcined once again at 700 °C for 24 h, re-ground, and subjected to a third calcination at 900 °C for another 24 h. The final product was pulverized and calcined further at 1150 °C for 24 h to ensure complete phase formation and enhanced crystallinity of the $BaNiO_3$ perovskite structure (Scheme 1).

2.5. Synthesis of $BaNiO_3$/g-C_3N_4 Composite

$BaNiO_3$/g-C_3N_4 composite was synthesized through a combined mechanical and sonochemical route to ensure uniform dispersion and strong interfacial interaction between both phases. Initially, 4g of g-C_3N_4 powder was ground manually using an agate mortar for 30 min to reduce its particle size and enhance surface reactivity. Subsequently, 1g of $BaNiO_3$ powder was added to the ground g-C_3N_4, and the mixture was further ground for an additional 30 min to obtain a homogeneous blend. The resulting powder was transferred to a 150 mL beaker, and a solvent mixture of 50 mL deionized water and 50 mL methanol was added. The suspension was stirred magnetically for 15 minutes to ensure proper wetting and dispersion, followed by ultrasonication for 30 minutes to achieve nanoscale mixing and exfoliation of g-C_3N_4 layers around $BaNiO_3$ particles. After ultrasonication, the suspension was dried at 75°C for 18 h to remove residual methanol, followed by further drying at 120°C for 2 h to eliminate water content. The obtained composite powder was stored in airtight vials for subsequent characterization and photocatalytic evaluation (Scheme 1).



Scheme 1. Green synthesis route of $BaNiO_3$ using *Peganum harmala* extract and the subsequent preparation of the $BaNiO_3$/g-C_3N_4 nanocomposite.

3. Results and discussions

3.1. Structural and morphological

The XRD patterns of the pristine g-C_3N_4, $BaNiO_3$, and $BaNiO_3$/g-C_3N_4 composite are shown in Fig. 1. The formation of pristine g-C_3N_4 is evidenced by the emergence of the typical diffraction peaks at 13.1 and 27.62º [41]. The weak

peak at 13.1° can be assigned to the (100) plane and is associated with the in-plane structural arrangement of the nitride layers, whereas the strong peak at 27.62° corresponds to the (002) reflection and originates from the periodic stacking of the layered aromatic g-C_3N_4 structure [42].

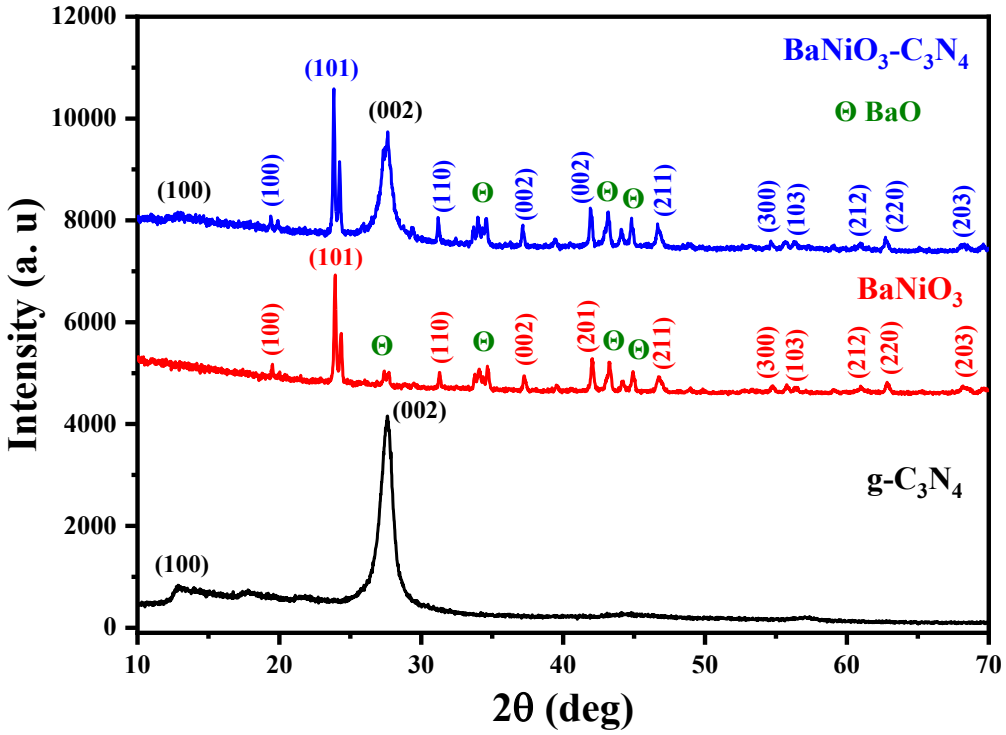


Figure 1. The XRD patterns of the synthesized nanostructures.

The XRD pattern of $BaNiO_3$ exhibits characteristic reflections at 19.00°, 23.82°, 31.27°, 37.22°, 39.50°, 42.13°, 43.26°, 44.92°, 46.92°, 54.70°, 55.77°, 56.42°, 62.78°, and 68.27°; the principal reflections are consistent with the hexagonal $BaNiO_3$ perovskite structure with P63mc symmetry (JCPDS no. 01-075-1201) [35, 43]. In addition, additional reflections attributable to $BaNiO_3$ are observed [44, 45], indicating the presence of a detectable secondary phase, possibly associated with incomplete reaction or an excess of the barium precursor. The XRD results support the formation of $BaNiO_3$ but do not establish phase purity. For the $BaNiO_3$/g-C_3N_4 composite, the characteristic diffraction features of both $BaNiO_3$ and g-C_3N_4 are observed, confirming the coexistence of the two components in the composite. However, some alterations occurred after incorporating the $BaNiO_3$ perovskite into the nitride matrix, such as a shift of the g-C_3N_4 (002) reflection toward lower diffraction angles, which may indicate an increase in the corresponding interlayer spacing [46, 47]. The structural variables including the crystallite size (D), dislocation density (δ), interlayer spacing (d), lattice parameters (a, b, c), and lattice strain (ε) are computed to evaluate the structural and

microstructural changes associated with composite formation, as summarized in Table 1. From the listed data, only limited variations in the calculated lattice parameters are observed, which could be related to local structural distortions, oxygen vacancies, point defects, or dislocation-related defects [48]. The increase in the g-C_3N_4 interlayer spacing may be related to interfacial interaction between $BaNiO_3$ and the layered g-C_3N_4 framework and/or local structural modification of the nitride layers [49-51].

Table 1. The microstructural parameters of the synthesized nanostructures

Variable	g-C_3N_4	$BaNiO_3$	$BaNiO_3$/g-C_3N_4	
			g-C_3N_4	$BaNiO_3$
$D = \frac{0.9\lambda}{\beta\, cos\theta}$ (nm)	8.82	59.65	10.57	62.83
$\delta = \frac{1}{D^2}$ (nm^{-2})	0.0129	0.0003	0.0090	0.0002
$d = \frac{\lambda}{2\, sin\theta}$ (nm)	0.3225	0.3717	0.3236	0.3729
$\frac{1}{d^2} = \frac{4}{3}\left(\frac{h^2+hk+k^2}{a^2}\right) + \frac{l^2}{c^2}$ (nm)	0.6450	a = 0.5711 c = 0.4833	0.6472	a = 0.5729 c = 0.4755
$\varepsilon = \frac{\beta}{4\tan\theta}$ (%)	0.0178	0.0028	0.0176	0.0024

The EDX spectra of the synthesized nanostructures are displayed in Fig. 2. The pristine g-C_3N_4 elemental composition consists mainly of C and N, in addition to traces of O. The C/N ratio was ≈ 0.85, which is higher than the stoichiometric ratio of 0.75 (Figs. 2 a-b). This deviation may be associated with structural and compositional changes occurring during thermal polymerization reactions. The low percentage of O may originate from surface oxygen-containing species. The EDX spectrum of $BaNiO_3$ (Figs. 2c-d) reveals the presence of Ba, Ni, and O, together with a trace of carbon signal. Considering that the $BaNiO_3$ precursor was subjected to high-temperature calcination, this carbon signal cannot be confidently attributed to residual plant-derived organic compounds and may instead originate from the carbon-containing mounting medium or carbon tape used during SEM-EDX analysis. Therefore, the carbon signal is not considered evidence of residual *Peganum harmala* extract. The formation of the $BaNiO_3$/g-C_3N_4 composite is verified by the coexistence of N, C, Ba, Ni, and O (Figs. 2e-f) indicating the merger of the $BaNiO_3$ perovskite and the g-C_3N_4. The morphology of the fabricated nanostructures is presented in Fig. 3. The pure g-C_3N_4 low magnification image (Fig. 3a) exhibits an aggregation beside many small particles. The formed aggregation has a rough surface, which might be due to the stacked structure of g-C_3N_4. From the low-magnification SEM image of $BaNiO_3$ (Fig. 3b), it is evident that $BaNiO_3$ nanoparticles have agglomeration and roughened surface, which may be associated with particle growth, crystallization, and aggregation during the high-temperature calcination process.

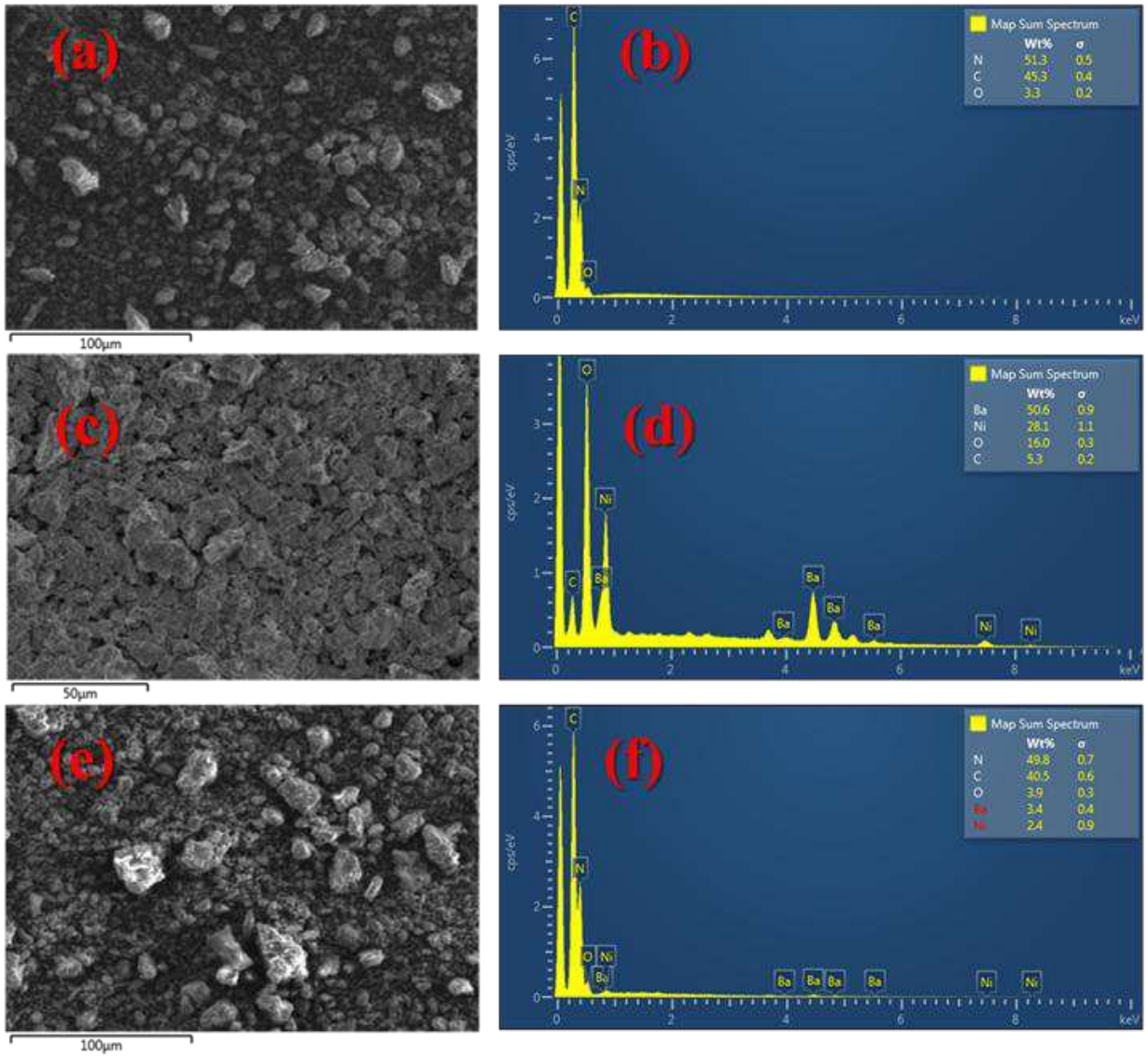


Figure 2. The EDX of g-C_3N_4 (a, b), $BaNiO_3$ (c, d), and $BaNiO_3$/g-C_3N_4 (e, f).

The SEM image of $BaNiO_3$/g-C_3N_4 (Fig. 3 c) shows morphological features associated with the two consistent materials, supporting their coexistence in the composite. The colored elemental mapping (Figs. 3(d–f) corresponding to the g-C_3N_4, $BaNiO_3$ and $BaNiO_3$/g-C_3N_4 shows the presence and spatial distribution of the constituent elements, which is consistent with EDX results.

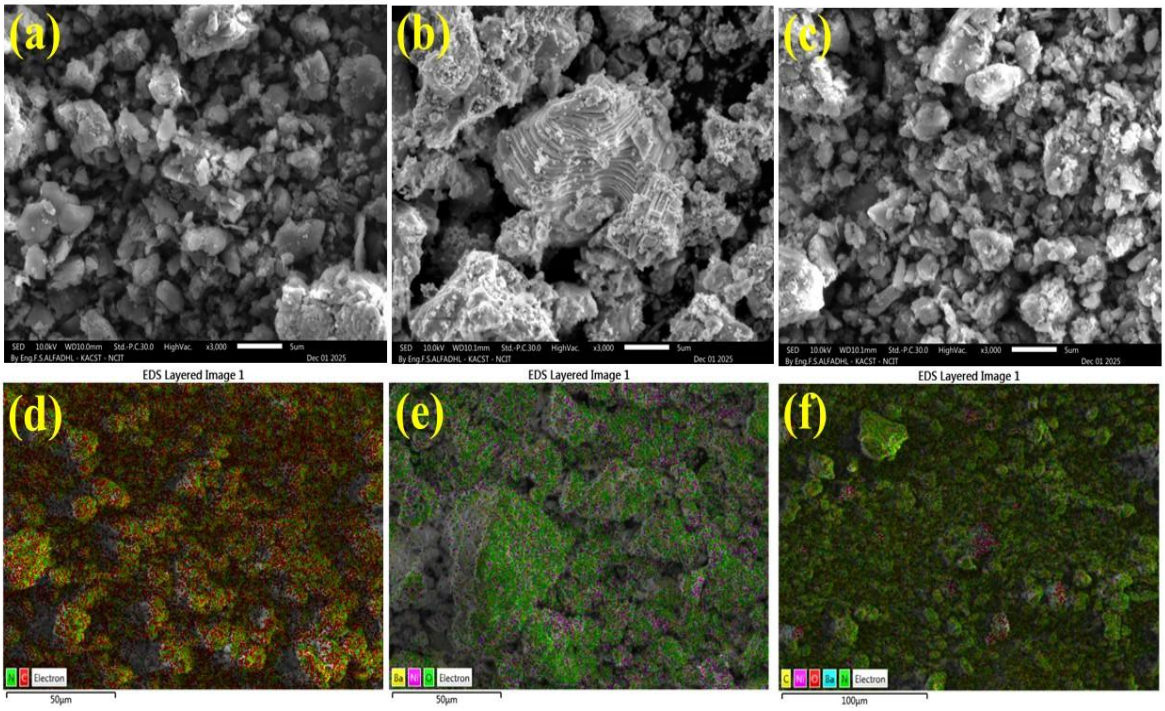


Figure 3. SEM and colored elemental mapping of pure g-C_3N_4, (a, d) $BaNiO_3$ (b, e), and $BaNiO_3$/g-C_3N_4 composite (c, f).

The TEM image of the g-C_3N_4 (Fig. 4a) displays stacked layers of nitride sheets as indicated by the dark contrast color of the image. Polygonal nanoparticles of about 100 to 200 nm size are shown by the TEM of the BaNiO3 perovskite (Fig. 4 b). The TEM of $BaNiO_3$/g-C_3N_4 composite (Figs. 4 c - d) exhibits BaNiO3 nanoparticles dispersed on a light contract color g-C_3N_4 sheets, thus confirming the anchoring of the $BaNiO_3$ to the g-C_3N_4 to form the composite.

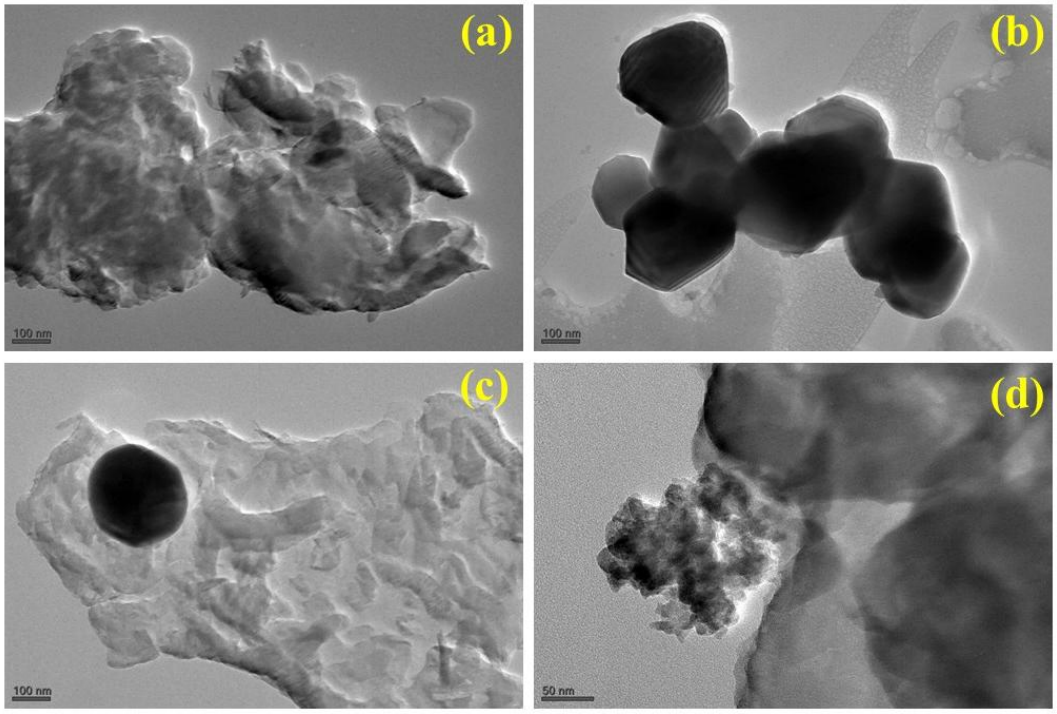


Figure 4. TEM of pure g-C_3N_4, (a) $BaNiO_3$ (b), and $BaNiO_3$/g-C_3N_4 composite (c).

FTIR analysis was performed to identify the characteristic functional groups in g-C_3N_4, $BaNiO_3$, and g-C_3N_4 /$BaNiO_3$ heterojunction (Fig. 5a). For $BaNiO_3$, the bands between 400–700 cm^{-1} can be attributed to Ba–O and Ni–O vibrations, while the band at 1431 cm^{-1} is associated with O–H bending on the surface [52]. In the g-C_3N_4 vibrations, the broad absorption band at 3080–3248 cm^{-1} corresponds to N–H/NH_2 stretching vibrations, whereas the bands observed at 1233–1636 cm^{-1} arise mainly from C–N and C=N vibrations within heterocyclic framework [30]. Additionally, the peaks at 800 and 876 cm^{-1} are ascribed to the breathing mode of the triazine units and N–H deformation [42]. After the $BaNiO_3$ and g-C_3N_4 there was prominent alteration in the wavenumbers as evidenced by the shift in the peaks towards higher wavenumber values indicating the insertion of the $BaNiO_3$ into the g-C_3N_4 matrix.

The DRS technique was employed to investigate the optical features of the samples. The DRS analysis findings have important implications in its photocatalytic activity. Hence, DRS analyses of the g-C_3N_4, $BaNiO_3$ and $BaNiO_3$/g-C_3N_4 were performed, and the findings are displayed in Figs5 b - d. Pristine has a band gap absorption edge of 415 nm which indicate its visible light absorption activity, where the $BaNiO_3$ band edge was 370nm making it less visible light active. The absorption edge of the $BaNiO_3$/g-C_3N_4 heterojunction shifted toward longer wavelengths, reaching

434nm, indicating enhanced visible light absorption after coupling $BaNiO_3$ with nitride. The optical band-gap energy was subsequently determined using the Tauc relation [53]:

$$\alpha h\nu = B\left(h\nu - E_g\right)^n \qquad (1)$$

In Tauc equation, α represents the absorption coefficient, h is the Planck's constant, ν denotes the photon frequency, Eg is the optical band-gap energy, and B is a proportionality constant. The exponent n depends on the type of the electronic transition, with values of 1/2 and 2 corresponding to direct and indirect transitions, respectively. The band-gap energy was determined from the intercept of the linear portion of the $(\alpha h\nu)^{1/2}$ versus hν plot with the energy axis, following the Tauc method [53]. At room temperature, the calculated Eg values were 2.89 eV for g-C_3N_4, 3.31 eV for $BaNiO_3$, and 2.86 eV for the $BaNiO_3$/g-C_3N_4 heterojunction (insets of Figs. 5b – d). Evidently, combining the g-C_3N_4 and $BaNiO_3$ led to the development of low band gap energy composite capable of efficient photocatalytic decomposition of organic dyes [54, 55]. Fig. 5e displays the PL emission spectra of the prepared g-C_3N_4, BaNiO3 and BaNiO3/g-C_3N_4 where the samples were excited by radiation with λexcitation = 325 nm. In the PL emission spectrum, g-C_3N_4 exhibited very high PL intensity, which is indicative of rapid recombination of the photogenerated holes and electrons [56, 57].

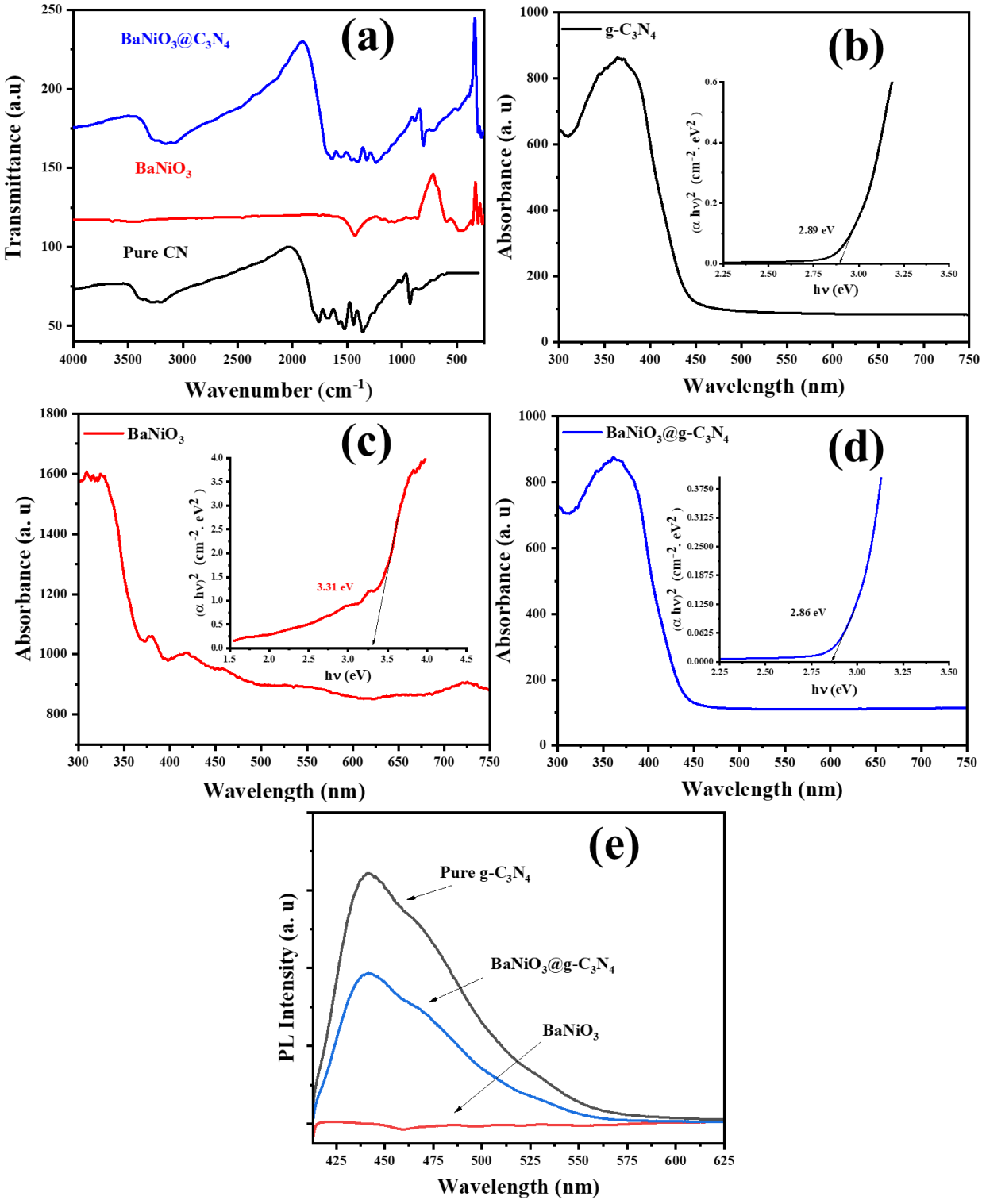


Figure 5. The FTIR spectra (a), UV-Vis and bandgap energy for g-C3N4 (b), $BaNiO_3$ (c), and g- $BaNiO_3$/g-C_3N_4 (d), and PL (e).

A look at the PL spectrum of the $BaNiO_3$/g-C_3N_4 composite divulges a diminution in the PL intensity, denoting that the charge carriers are effectively parted, preventing the recombination of the photogenerated electron–hole pairs [58, 59]. Facile generation of the electron–hole pair, along with the high conductivity of g-C_3N_4 is expected to promote better efficiency of the photocatalytic degradation. Furthermore, the interfacial amalgamation between g-C_3N_4 and BaNiO3 in BaNiO3/g-C_3N_4 created an appropriate heterojunction, which was also advantageous for charge separation, thus boosting the photocatalytic performance [60]. The PL spectrum of g-C_3N_4 exhibited a stronger emission than that of $BaNiO_3$, which showed a comparatively weaker signal, suggesting more effective charge-carrier separation in the latter. A similar behavior was reported by Kalidasan et al. [61], who observed that WO_3 exhibited more efficient charge-carrier transfer than g-C_3N_4, as evidenced by its weaker PL emission.

3.2. Photocatalytic Degradation

The photocatalytic removal of AB dye was evaluated under visible light irradiation for up to 75 min at room temperature. Experiments were conducted in a 250 mL Pyrex glass reactor containing 100 mL of 50 ppm AB solution and 50 mg of photocatalyst under continuous magnetic stirring. Before illumination, the suspension was kept in the dark for 30 min to establish adsorption-desorption equilibrium. Visible-light irradiation was provided by a TOSHIBA LDA14L-G/100W lamp equipped with a UV cutoff filter (Y-44, HOYA) to exclude wavelengths below 400 nm. The lamp was positioned above the reactor during irradiation; however, the irradiance at the reactor surface, photon flux, and wavelength-resolved spectral distribution after the cutoff filter were not directly measured in the present study. Therefore, these parameters are not reported as quantitative values. The nominal lamp specification is reported as provided by the manufacturer and should not be interpreted as the actual optical power delivered to the reactor. The reaction was conducted at room temperature, although the temperature variation during irradiation was not independently monitored. At 10 min intervals, 5 mL aliquots were collected and centrifuged at at 10,000 rpm for 5 min to remove the photocatalyst. The residual AB concentration was determined from the supernatant using a UV-vis spectrophotometer at its maximum absorption wavelength (λmax = 596 nm). A photolysis experiment without photocatalyst was also performed under identical conditions for comparison.

The degradation kinetics were analyzed using the Langmuir–Hinshelwood (L–H) model developed by Turchi and Ollis [62], expressed as:

$$r_0 = -\frac{dC}{dt} = \frac{kKC}{1+KC} \quad (2)$$

In this equation, r0 denotes the initial degradation rate, k represents the reaction rate constant, while K and C correspond to the adsorption equilibrium constant and reactant concentration, respectively. When the initial reactant concentration (C_0) is sufficiently low, its expression can be reduced to:

$$ln\frac{(C_0)}{C_t} = kKt = k_{obs}t \quad (3)$$

During photocatalytic degradation, the relative absorbance of AB (At/A0) can be used to represent the corresponding change in dye concentration (Ct/C0), assuming the Beer–Lambert law applies. The calculated degradation percentage (Figs. 6a – c) were 6, 58.7, 37.3, and 94.2 % for photolysis, g-C_3N_4, $BaNiO_3$ and BaNiO3/g-C3N4, respectively. The insignificant degradation through photolysis indicated the stability of the AB dye and reflect the role of the prepared naonstructure in the process [63]. The linear relationship between ln(A/A0) and irradiation time (t) confirms that AB degradation follows pseudo-first-order kinetics (Fig. 6b) [64]. The $BaNiO_3$/g-C_3N_4 composite exhibited a rate constant (k1) of 0.0273 min–1, approximately 5 and 25 times higher than those of g-C_3N_4 and $BaNiO_3$, respectively (Table 2).

Table 2. The kinetics parameters of the visible light driven AB dye photodegradation by BaNiO3/g-C3N4

Photocatalyst	$t_{1/2}$ (min)	k_1 (min^{-1})	R^2	RSS
Photolysis	990	0.0007	0.9150	0.0003
Pure g-C_3N_4	126	0.0055	0.9851	0.0029
$BaNiO_3$	630	0.0011	0.9994	0.0004
$BaNiO_3$/g-C_3N_4	25.4	0.0273	0.9928	0.0345

The corresponding half-life, calculated from $t_{1/2} = ln2/k_1$, was about 25 min, further demonstrating the superior photocatalytic efficiency of composite [65]. The relatively high degradation activity of the composite could be related to the lower band gap energy, the efficient charge carriers' separation (PL analysis). The influence of experimental parameters; AB dye concentration, photocatalyst dose and medium pH were explored to determine the optimal conditions for the degradation process. 50, 100, and 200 ppm of the dye were used to test the effect of the amount of dye of the degradation as shown in Figs. 6(d, e). The degradation percentage was 94.2, 67.3, and 55.3 % when the 50,

100, 1nd 200 ppm were respectively used. The decrease in the photodegradation percentage with the rise in the colored dye concentration may be due to the screening effect of the dye color that restricts the radiation from reaching the photocatalyst surface [66].

The uploading of photocatalyst provides more pore site for the adsorption of the dye molecules before getting destroyed. This is manifested by the increase of adsorption rate from 56, 64.8, 77.3 and 94.3 % when the $BaNiO_3$/g-C_3N_4 dose was respectively 10, 20,30, and 50 mg (Fig. 6f). The maximum activity was attained using 50 mg of the catalyst as beyond this threshold the solid nanoparticles get agglomerated and the adsorption sites are blocked [67].
The influence of solution pH on AB degradation was investigated at pH = 3, 5, 7, 9, and 11, as depicted in Fig. 7a. The maximum degradation was achieved when the solution pH was 7. At pH below 7 the amino groups of the composite and the sulfonate get protonated which lead to a repulsion that reduce the photodegradation [68]. This effect is more pronounced pH = 3 which is highly acidic. On the other hand, at pH 9 and 11 the anionic AB dye repulsion with the OH- covered photocatalyst minimizes the degradation percentage [69]. Hence, pH = 7 was found to be the best for the AB dye degradation. To delineate the active species in control for the photocatalytic degradation of AB dye, a sequence of radical quenching tests [70] were carried out employing certain scavengers Fig. 7b.

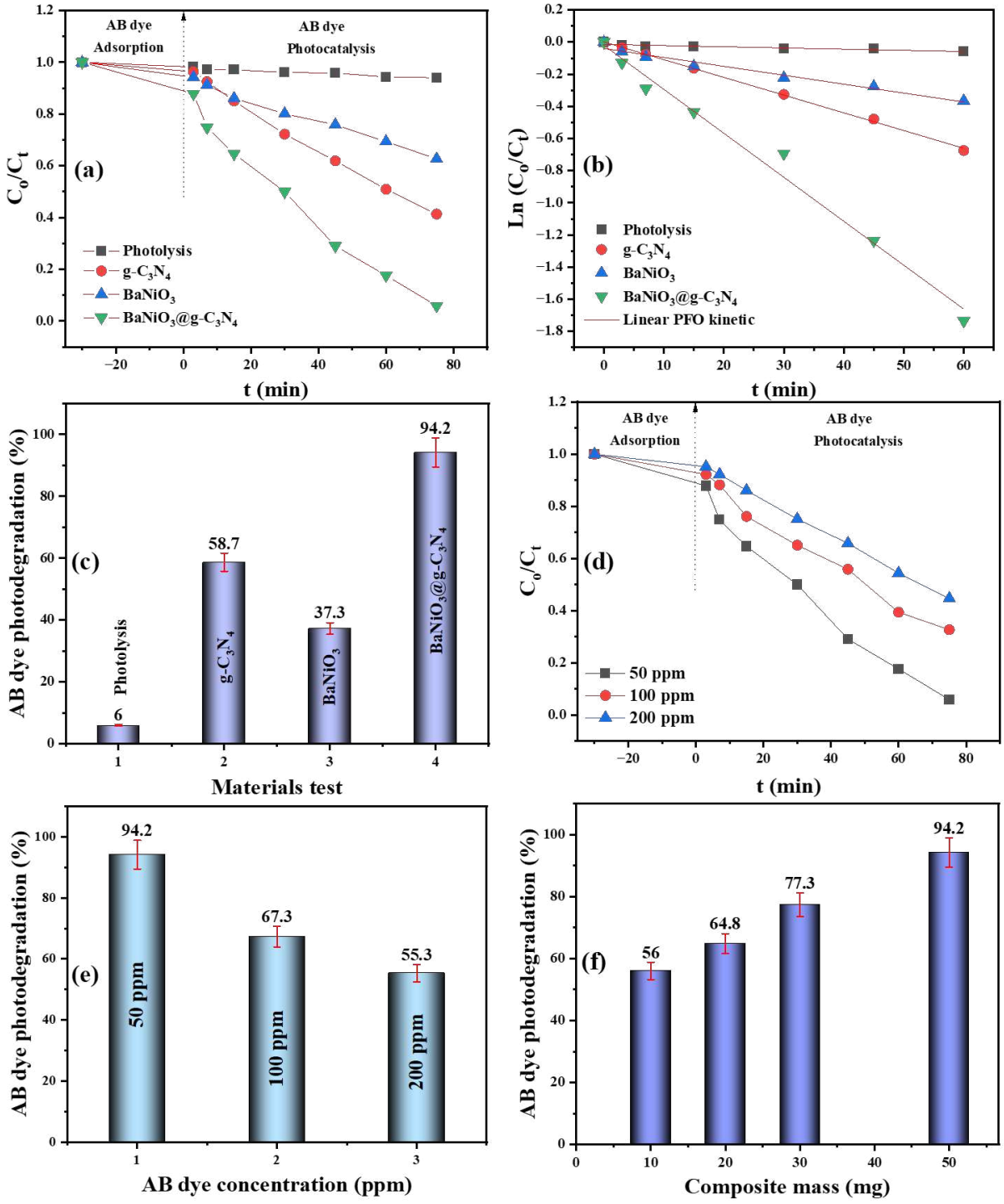


Figure 6. The photocatalytic efficiency (a, c), adsorption kinetics (b). effect of AB concentration (d, e), and composite dose (f) on the AB photodegradation.

The scavengers employed in the study included EDTA to quench photogenerated holes (h^+), isopropanol (IPA) to capture (•OH), $AgNO_3$ to trap photogenerated electrons, and ascorbic acid (ASC) to scavenge superoxide radicals ($^{\bullet}O^{2-}$) [71, 72]. Among them, EDTA and ASC exhibited the utmost repressive influence on the degradation efficacy by sequentially decreasing the degradation rate to 18.8 and 21.5 % from 94.2 %, inferring that (h^+) and $^{\bullet}O^{2-}$ were the leading reactive species in the photocatalytic process. A considerable effect of the IPA on diminishing the photodegradation to 49.8 % which indicate the moderate involvement of the ($^{\bullet}OH$) radical in the degradation process [73, 74]. The very minor decrease in the degradation process (≈10 %) indicates no direct role of the electrons in the process.

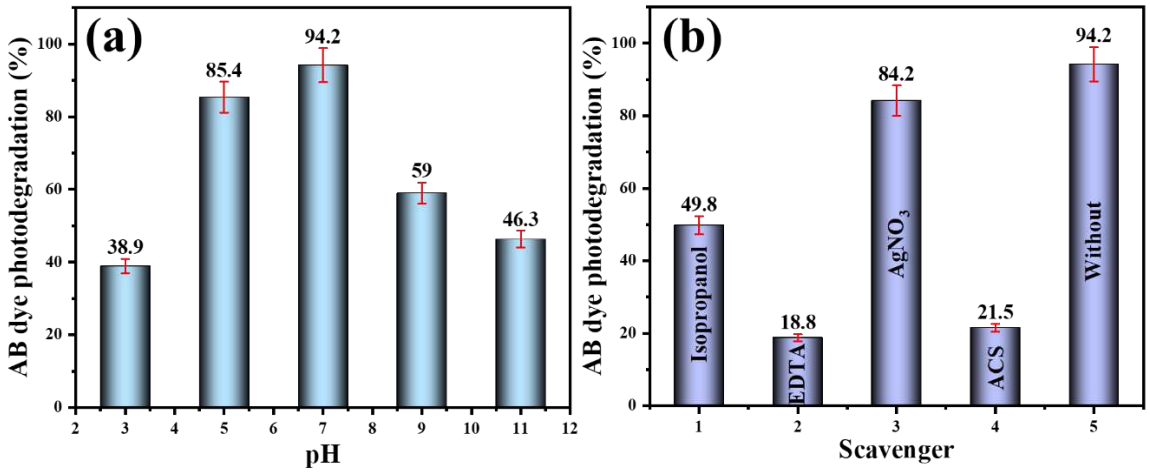


Figure 7. The pH effect (a) and scavengers' tests (b) on the AB photodegradation.

Table 3 compares of the photocatalytic efficiency of the $BaNiO_3$/g-C_3N_4 composite developed in this study with various photocatalysts reported in the literature for the degradation of azo dyes. As can be observed, the $BaNiO_3$/g-C_3N_4 heterostructure exhibits a higher apparent reaction rate constant (0.0273 min^{-1}) under visible-light irradiation than several previously reported photocatalysts, including those operating under UV irradiation. Furthermore, the degradation process was achieved within a relatively short reaction time and under environmentally friendly condition (pH7), highlighting the practical applicability of the developed material for wastewater treatment.

The superior photocatalytic performance of $BaNiO_3$/g-C_3N_4 is mainly associated with the establishment of a direct Z-scheme heterojunction at $BaNiO_3$/g-C_3N_4 interface. This heterostructure facilitates the efficient separation and migration of photogenerated charge carriers while preserving the strong redox potential and directional transfer of photogenerated charge carriers while maintaining the strong reduction and oxidation capabilities of the two semiconductor components. As a result, the recombination of photogenerated electron-hole pairs is markedly

inhibited, thereby favoring the formation of reactive oxygen species, particularly $^{\bullet}OH$ and $^{\bullet}O^{2-}$, which contribute substantially to the degradation of the dye. In addition, the intimate interfacial contact, enlarged active surface area, and synergistic adsorption-photocatalysis effect contribute to the remarkable performance of the composite compared with many conventional photocatalysts reported in the literature.

The proposed photocatalytic degradation mechanism of the BaNiO3/g-C3N4 nanocomposite is based on the respective valence-band (VB) and conduction-band (CB) positions of $BaNiO_3$ and g-C_3N_4, which were estimated employing the Butler-Ginley equation [85]:

$$E_{VB} = X - E_c + 0.5E_g \quad (4)$$

$$E_{CB} = E_{VB} - E_g \quad (5)$$

Here, (E_c) denotes the energy of a free electron on the hydrogen scale, while (X) represents the absolute Mulliken electronegativity of the semiconductor. The absolute electronegativity of BaNiO3 was calculated using the formula $X_{BaNiO3} = \sqrt[5]{X_{Ba}^1 . X_{Ni}^1 . X_O^3}$ where the absolute

electronegativity for the Ba, Ni, and O is respectively 2.4, 4.4, and 7.54 and it was found to be 5.385. For the g-C3N4 the X is 4.73. The VB and CB for the BaNiO3 were 2.54 and - 0.77 eV respectively, where g-C3N4 has VB = 1.675 eV and CB = - 1.215 eV.

Table 3. A comparison of the AB dye photodegradation by $BaNiO_3$/g-C_3N_4 with other nanostructures.

Catalyst	pH	Dye (ppm)	Kinetic	Rate (min^{-1})	Source	Ref.
ZnO/CuO/GO	6	150	PFO	0.0235	UV	[75]
$CoFe_2O_4$	7	10	PFO	0.0132	Solar	[76]
$BiPO_4$	-	20	PFO	0.0113	UV	[77]
TiO_2/Anthocyanins	3	1 mM	PFO	0.0035	UV	[78]
SnO_2	5.6	100	PFO	0.0171	UV	[79]
TiO_2	3	1 mM	PFO	0.0038	Visible	[78]
g-C_3N_4	7	50	PFO	0.0098	Visi.	[80]
$BiVO_4$	7	20	PFO	0.0154	Vis.	[81]
ZnO/ g-C_3N_4	7	25	PFO	0.0197	Vis.	[82]
Ag_3PO4/ g-C_3N_4	6.5	20	PFO	0.0216	Vis.	[83]
Bi_2WO_6/ g-C_3N_4	7	20	PFO	0.0245	Vis.	[84]
$BaNiO_3$/g-C_3N_4	7	50	PFO	0.0273	Vis.	This work

Based on the scavenger experiments and the estimated EvB and ECB values of $BaNiO_3$ and g-C_3N_4, the photocatalytic degradation of AB dye is proposed to proceed through a Z-scheme charge-transfer mechanism [86], as schematically illustrated in Fig. 8. This mechanism is supported by the suitable band positions of the two semiconductors: the conduction-band (CB) potential of g-C_3N_4 is sufficiently negative to reduce O_2, whereas the valence-band (VB) potential of $BaNiO_3$ is sufficiently positive to promote the oxidation of H_2O to ·OH. Upon visible-light irradiation, both $BaNiO_3$ and g-C_3N_4 are photoexcited, generating electrons in their respective CBs and holes in their VB, respectively [87, 88]. Owing to the favorable energetic alignment between CB of BaNiO3 and the VB of g-C_3N4 electrons from the $BaNiO_3$ CB can recombine preferentially with holes in the and the g-C_3N_4 VB. This selective interfacial charge transfer constitutes the characteristic Z-scheme pathway in the $BaNiO_3$/g-C_3N_4 heterojunction, thereby preserving the highly reducing electrons and strongly oxidizing holes while enhancing the spatial separation of the remaining charge carriers [89, 90].

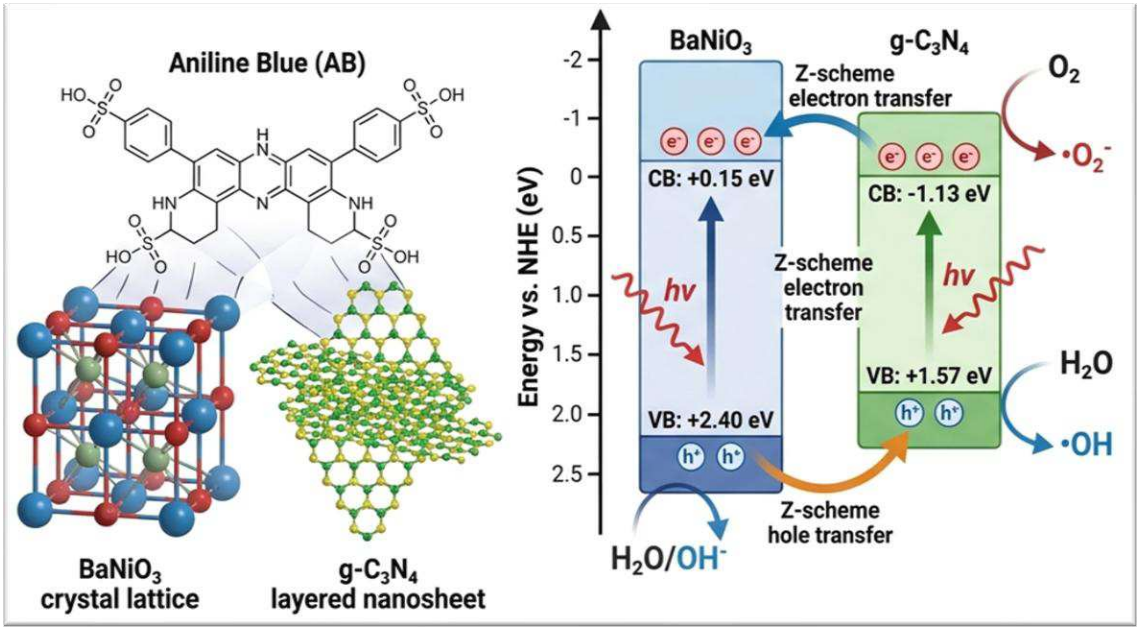


Figure 8. The proposed Z-scheme for the AB dye degradation.

At pH=7, The standard redox potential for superoxide radical ($^{\bullet}O^{2-}$) generation is approximately −0.033 eV versus the normal hydrogen electrode (NHE); hence, the CB potential of the photocatalyst should be more negative than this value to enable O_2 reduction to $^{\bullet}O^{2-}$ [91]. In contrast, the generation of $^{\bullet}$OH requires a highly positive potential of approximately +2.3 V versus NHE at pH 7 [92]. Accordingly, the photoexcited electrons located in the CB of g-C_3N_4

can reduce dissolved O_2 to produce $^{\bullet}O^{2-}$ species. Conclusively, coupling g-C3N4 with $BaNiO_3$ to form heterojunction facilitates interfacial charge migration, provides a greater number of accessible surface-active sites, and consequently enhances the photocatalytic degradation performance. The generated holes (h^+) can immediately interact with the OH^- in the solution, to form $^{\bullet}OH$ radicals, the dissolved O_2 in solution may absorb the formed electron (e^-) and change into ($^{\bullet}O^{2-}$), the superoxide ion ($^{\bullet}O^{2-}$) can react to form the $^{\bullet}OH$ radicals [93, 94]. The reactive radicals $^{\bullet}O^{2-}$ and $^{\bullet}OH$ degrade the dye molecules [95]:

$$h^+ + OH^- \rightarrow OH^{\cdot}$$

$$e^- + O_2 \rightarrow O_2^{\cdot -}$$

$$O_2^{\cdot -} + H^+ \rightarrow H_2O^{\cdot}$$

$$2H_2O^{\cdot} \rightarrow O_2 + H_2O_2$$

$$H_2O_2 + O_2^{\cdot -} + \rightarrow OH^{\cdot} + O_2 + OH^-$$

$$OH^{\cdot}/O_2^{\cdot -} + dye \rightarrow dye\ degradation\ products$$

4. Conclusions

In this study, a $BaNiO_3$/g-C_3N_4 heterojunction nanocomposite was successfully developed from $BaNiO_3$ and pristine g-C_3N_4 and evaluated for the visible-light-driven degradation of AB dye. The resulting photocatalyst achieved 94% degradation of AB within 80 min, demonstrating enhanced photocatalytic activity compared with the individual components. This improvement was primarily associated with the formation of the $BaNiO_3$/g-C_3N_4 heterojunction, which can facilitate interfacial charge separation and reduce electron-hole recombination, consistent with the PL results. The apparent reaction rate constant of the $BaNiO_3$/g-C_3N_4 was approximately 25 and 5 times higher than those of pristine $BaNiO_3$ and g-C_3N_4, respectively. Radical scavenging experiments further confirmed the importance of $^{\bullet}OH$ and $^{\bullet}O^{2-}$ reactive species in AB degradation. The findings demonstrate that constructing a $BaNiO_3$/g-C_3N_4 heterojunction is a promising strategy for improving visible-light photocatalytic performance and demonstrates potential for dye-contaminated water treatment.

Author Contributions: Conceptualization, M.S.A. and A.M.; methodology, M.S.A., M.A.A. F.M.A. and A.A.; software, M.S.A., M.A.A. F.M.A., A.M., F.A. and M.K.; validation, A.M., F.A. and M.K.; formal analysis, M.S.A., M.A.A. F.M.A. and A.A.; investigation, A.M., F.A. and M.K.; data curation, A.M., F.A. and M.K.; writing—original draft preparation, M.S.A., A.A., A.M. and M.K.; writing—review and editing, A.M., F.A. and M.K.; visualization, A.M., F.A. and M.K.; supervision, A.M. and M.K. All authors have read and agreed to the published version of the manuscript.
Institutional Review Board Statement: Not applicable.
Informed Consent Statement: Not applicable.
Data Availability Statement: Data are available within the article.
Conflicts of Interest: Declare conflicts of interest or state.

References

1. Vinayagam, V.; Palani, K.N.; Ganesh, S.; Rajesh, S.; Akula, V.V.; Avoodaiappan, R.; Kushwaha, O.S.; Pugazhendhi, A. Recent developments on advanced oxidation processes for degradation of pollutants from wastewater with focus on antibiotics and organic dyes. *Environ. Res.* 2024, *240*, 117500.

2. Lan, D.; Zhu, H.; Zhang, J.; Li, S.; Chen, Q.; Wang, C.; Wu, T.; Xu, M. Adsorptive removal of organic dyes via porous materials for wastewater treatment in recent decades: A review on species, mechanisms and perspectives. *Chemosphere* 2022, *293*, 133464.

3. Rajak, P.; Ganguly, A.; Nanda, S.; Mandi, M.; Ghanty, S.; Das, K.; Biswas, G.; Sarkar, S. Toxic contaminants and their impacts on aquatic ecology and habitats. In *Spatial Modeling of Environmental Pollution and Ecological Risk*; Elsevier: Amsterdam, The Netherlands, 2024; pp. 255–273.

4. Hansen, H.C.B.; Hilscherova, K.; Bucheli, T.D. Natural toxins: Environmental contaminants calling for attention. *Environ. Sci. Eur.* 2021, *33*, 112.

5. Thompson, L.A.; Darwish, W.S. Environmental chemical contaminants in food: Review of a global problem. *J. Toxicol.* 2019, *2019*, 2345283.

6. Ben Mbarek, W.; Daza, J.; Escoda, L.; Fiol, N.; Pineda, E.; Khitouni, M.; Suñol, J.-J. Removal of Reactive Black 5 azo dye from aqueous solutions by a combination of reduction and natural adsorbents processes. *Metals* 2023, *13*, 474. https://doi.org/10.3390/met13030474.

7. Hanafi, M.F.; Sapawe, N. A review on the current techniques and technologies of organic pollutants removal from water/wastewater. *Mater. Today Proc.* 2020, *31*, A158–A165.

8. Chen, X.; Liu, L.; Feng, Y.; Wang, L.; Bian, Z.; Li, H.; Wang, Z.L. Fluid eddy induced piezo-promoted photodegradation of organic dye pollutants in wastewater on ZnO nanorod arrays/3D Ni foam. *Mater. Today* 2017, *20*, 501–506.

9. Alzain, H.; Kalimugogo, V.; Hussein, K.; Karkadan, M. A review of environmental impact of azo dyes. *Int. J. Res. Rev.* 2023, *10*, 673–689.

10. Zhu, X.; An, S.; Liu, Y.; Hu, J.; Liu, H.; Tian, C.; Dai, S.; Yang, X.; Wang, H.; Abney, C.W. Efficient removal of organic dye pollutants using covalent organic frameworks. *AIChE J.* 2017, *63*, 3470–3478.

11. Aliyev, I.A.; Trofimov, B.A.; Oparina, L.A. *Aromatic Thiols and Their Derivatives*; Springer Nature: Cham, Switzerland, 2021.

12. Wang, Y.X.; Wang, J.; Mou, L.L.; Zhang, H.Z.; Chen, G.Y.; Zhou, C.H. Comprehensive insights into sulfanilamido-based medicinal design and research. *Med. Res. Rev.* 2025, *45*, 1700–1817.

13. Nayna, O.K.; Tareq, S.M. Application of semiconductor nanoparticles for removal of organic pollutants or dyes from wastewater. In *Nanotechnology in Water and Wastewater Treatment*; Elsevier: Amsterdam, The Netherlands, 2019; pp. 267–290.

14. Shen, Z.; Xu, B.; Liu, P.; Hu, Y.; Yu, Y.; Ding, H.; Kloo, L.; Hua, J.; Sun, L.; Tian, H. High performance solid-state dye-sensitized solar cells based on organic blue-colored dyes. *J. Mater. Chem. A* 2017, *5*, 1242–1247.

15. Hanafi, M.F.; Sapawe, N. A review on the water problem associate with organic pollutants derived from phenol, methyl orange, and remazol brilliant blue dyes. *Mater. Today Proc.* 2020, *31*, A141–A150.

16. Ben Mbarek, W.; Pineda, E.; Escoda, L.; Suñol, J.-J.; Khitouni, M. High efficiency decolorization of azo dye Reactive Black 5 by Ca-Al particles. *J. Environ. Chem. Eng.* 2017, *5*, 6107–6113. https://doi.org/10.1016/j.jece.2017.11.032.

17. Priya, A. Utilization of waste materials as adsorbents for color removal from textile effluents—A review. *Biomed. J.* 2018, *2(2), 1-3*. https://doi.org/10.26717/BJSTR.2018.02.000719

18. Kolya, H.; Kang, C.-W. Toxicity of metal oxides, dyes, and dissolved organic matter in water: Implications for the environment and human health. *Toxics* 2024, *12*, 111.

19. Abbasi, A.; Alothaid, H.; Al-Haider, S.M.; Ikram, S. Efficient removal of Janus green and aniline blue dyes from aqueous medium via tryptophan functionalized Gellan gum-cl-β-cyclodextrin/CeO_2 nanocomposite. *Int. J. Biol. Macromol.* 2025, *308*, 142399.

20. Zhang, C.; Huang, Y.; He, J.; He, L.; Zhang, J.; Yu, L.; Musazade, E.; Maser, E.; Xiong, G.; Xu, M. The mechanism of aniline blue degradation by short-chain dehydrogenase (SDRz) in *Comamonas testosteroni*. *Molecules* 2024, *29*, 5405.

21. Eswaran, S.G.; Narayan, H.; Vasimalai, N. Reductive photocatalytic degradation of toxic aniline blue dye using green synthesized banyan aerial root extract derived silver nanoparticles. *Biocatal. Agric. Biotechnol.* 2021, *36*, 102140.

22. Das, A.; Rani, P.; Ghosh Dastider, S.; Kanta Mondal, K.; Alegaonkar, P.S. An experimental and theoretical investigation on highly reusable visible light active CoTe nanosheets for improved photocatalytic degradation of toxic aniline blue dye. *ChemistrySelect* 2024, *9*, e202400032.

23. Usman, M.; Aftab, R.; Zaidi, S.; Adnan, S.; Rao, R. Adsorption of aniline blue dye on activated pomegranate peel: Equilibrium, kinetics, thermodynamics and support vector regression modelling. *Int. J. Environ. Sci. Technol.* 2022, *19*, 8351–8368.

24. Gopalakrishnan, G.; Jeyakumar, R.B.; Somanathan, A. Challenges and emerging trends in advanced oxidation technologies and integration of advanced oxidation processes with biological processes for wastewater treatment. *Sustainability* 2023, *15*, 4235.

25. Gaur, B.; Mittal, J.; Hassan, H.; Mittal, A.; Baker, R.T. Ordered mesoporous carbon as adsorbent for the removal of a triphenylmethane dye from its aqueous solutions. *Molecules* 2024, *29*, 4100.

26. Ghernaout, D.; Elboughdiri, N. Advanced oxidation processes for wastewater treatment: Facts and future trends. *Open Access Libr. J.* 2020, *7*, 1–15.

27. Pandis, P.K.; Kalogirou, C.; Kanellou, E.; Vaitsis, C.; Savvidou, M.G.; Sourkouni, G.; Zorpas, A.A.; Argirusis, C. Key points of advanced oxidation processes (AOPs) for wastewater, organic pollutants and pharmaceutical waste treatment: A mini review. *ChemEngineering* 2022, *6*, 8.

28. Mahbub, P.; Duke, M. Scalability of advanced oxidation processes (AOPs) in industrial applications: A review. *J. Environ. Manag.* 2023, *345*, 118861.

29. Thakurata, D.G.; Das, K.C.; Dhar, S.S. Efficient photocatalytic degradation of aniline blue under solar irradiation by ternary cobalt ferrite/graphitic carbon nitride/bentonite nanocomposite. *Environ. Sci. Pollut. Res.* 2022, *29*, 34269–34277.

30. Naveed, A.B.; Javaid, A.; Zia, A.; Ishaq, M.T.; Amin, M.; Farooqi, Z.U.R.; Mahmood, A. TiO_2/g-C_3N_4 binary composite as an efficient photocatalyst for biodiesel production from Jatropha oil and dye degradation. *ACS Omega* 2023, *8*, 2173–2182.

31. Yu, Y.; Huang, H. Coupled adsorption and photocatalysis of g-C_3N_4-based composites: Material synthesis, mechanism, and environmental applications. *Chem. Eng. J.* 2023, *453*, 139755.

32. Zhao, G.-Q.; Zou, J.; Hu, J.; Long, X.; Jiao, F.-P. A critical review on graphitic carbon nitride (g-C_3N_4)-based composites for environmental remediation. *Sep. Purif. Technol.* 2021, *279*, 119769.

33. Lee, J.G.; Hwang, J.; Hwang, H.J.; Jeon, O.S.; Jang, J.; Kwon, O.; Lee, Y.; Han, B.; Shul, Y.-G. A new family of perovskite catalysts for oxygen-evolution reaction in alkaline media: $BaNiO_3$ and $BaNi_{0.83}O_{2.5}$. *J. Am. Chem. Soc.* 2016, *138*, 3541–3547.

34. Durmus, Z.; Köferstein, R.; Lindenberg, T.; Lehmann, F.; Hinderberger, D.; Maijenburg, A.W. Preparation and characterization of Ce-MOF/g-C_3N_4 composites and evaluation of their photocatalytic performance. *Ceram. Int.* 2023, *49*, 24428–24441.

35. Janjua, A.N.; Ahmed, A.; Singh, A.; Sundramoorthy, A.K.; Young, S.J.; Chu, Y.L.; Arya, S. Synthesis, characterization, and implementation of $BaNiO_3$ perovskite nanoparticles as thin film supercapacitor electrode. *Energy Storage* 2024, *6*, e630.

36. Manj, R.M.A.K.; Ramay, S.M.; Shar, M.; Naseem, S.; Atiq, S. Optimization of switching charge and recoverable energy density mediated by structural transformation in Sr-substituted $BaNiO_3$ perovskites. *RSC Adv.* 2024, *14*, 15791–15803.

37. Gutiérrez-Martín, D.; Varela, Á.; Torres-Pardo, A.; Hernando, M.; Matesanz, E.; González-Calbet, J.M.; Portehault, D.; Parras, M. $BaNiO_3$ electrocatalysts for oxygen evolution reaction: The role of synthetic methods. *Inorg. Chem.* 2025, *64*, 18385–18393.

38. Lee, J.G.; Hwang, H.J.; Kwon, O.; Jeon, O.S.; Jang, J.; Shul, Y.-G. Synthesis and application of hexagonal perovskite $BaNiO_3$ with quadrivalent nickel under atmospheric and low-temperature conditions. *Chem. Commun.* 2016, *52*, 10731–10734.

39. Zhu, Z.; Zhao, S.; Wang, C. Antibacterial, antifungal, antiviral, and antiparasitic activities of *Peganum harmala* and its ingredients: A review. *Molecules* 2022, *27*, 4161.

40. Jabeen, I.; Rashid, Z.; Waheed, R.; Zafar, S.; Ahmad, K.; Arooj, I.; Aleem, A.; Batool, S.; Islam, N.; Ahmad, I. Green synthesis and biological applications of *Peganum harmala* mediated copper oxide nanoparticles. *J. Mol. Struct.* 2025, *1325*, 140838.

41. Basaleh, A.; Mahmoud, M. $CoAl_2O_4$–g-C_3N_4 nanocomposite photocatalysts for powerful visible-light-driven hydrogen production. *ACS Omega* 2021, *6*, 10428–10436.

42. Kaçar, N.; Çayirli, M.; Ozden, R.C.; Lokcu, E.; Anik, M. Photocatalytic efficiency of g-C_3N_4/graphene nanocomposites in the photo-assisted charging of the Li-ion oxygen battery. *ACS Omega* 2023, *8*, 46227–46235.

43. Choi, J.-Y.; Cho, J.-H.; Sun, J.-W.; Kim, H.-P.; Ryu, J.; Durmus, Y.E.; Tempel, H.; Eichel, R.-A.; Jo, W. Morphology control of high-quality hexagonal perovskite $BaNiO_3$ by molten salt method. *Mater. Today Chem.* 2023, *32*, 101645.

44. Ansari, M.A.; Jahan, N. Structural and optical properties of BaO nanoparticles synthesized by facile co-precipitation method. *Mater. Highlights* 2021, *2*, 23–28.

45. Zhang, W.; Wang, S.; Li, S.; Lu, L.; Cheng, X. Effect of BaO on the calcination and hydration characteristic of CA. *J. Therm. Anal. Calorim.* 2019, *136*, 1481–1488.

46. Kesari, S.; Garg, A.B.; Clemens, O.; Joseph, B.; Rao, R. Pressure-induced structural behavior of orthorhombic $Mn_3(VO_4)_2$: Raman spectroscopic and X-ray diffraction investigations. *ACS Omega* 2022, *7*, 3099–3108.

47. He, L.; Polsin, D.; Zhang, S.; Collins, G.W.; Abdolrahim, N. Phase transformation path in aluminum under ramp compression: Simulation and experimental study. *Sci. Rep.* 2022, *12*, 18954.

48. Malebadi, K.A.; Seheri, N.H.; Ojelere, O.; Onwudiwe, D.C. ZnO nanoparticles modified with g-C_3N_4: Optical and structural properties. *Mater. Sci. Eng. B* 2024, *310*, 117676.

49. Durairaj, A.; Sakthivel, T.; Ramanathan, S.; Vasanthkumar, S. Quenching-induced structural distortion of graphitic carbon nitride nanostructures: Enhanced photocatalytic activity and electrochemical hydrogen production. *ACS Omega* 2019, *4*, 6476–6485.

50. Wang, T.; Tian, H.; Lv, T.; Li, C.; Wang, D.; Zhang, Z.; Guo, M.; Li, Z. Investigating the lateral expansion, molecular adsorption, and photocatalytic behavior of 2D graphitic carbon nitride (g-C_3N_4) planes. *J. Environ. Chem. Eng.* 2025, *13*, 117409.

51. Vu, N.N.; Nguyen, C.C.; Kaliaguine, S.; Do, T.O. Synthesis of g-C_3N_4 nanosheets by using a highly condensed lamellar crystalline melamine–cyanuric acid supramolecular complex for enhanced solar hydrogen generation. *ChemSusChem* 2019, *12*, 291–302.

52. Ahmad, N.; Wahab, R.; Manoharadas, S.; Alrayes, B.F.; Alharthi, F. Utilization of greenhouse gases for syngas production by dry reforming process using reduced $BaNiO_3$ perovskite as a catalyst. *Sustainability* 2021, *13*, 13855.

53. Mukhopadhyay, A.K.; Momin, M.A.; Roy, A.; Das, S.C.; Majumdar, A. Optical and electronic structural properties of Cu_3N thin films: A first-principles study (LDA+U). *ACS Omega* 2020, *5*, 31918–31924.

54. Feng, Y.; Liu, L.; Chen, P.; Bo, M.; Xie, J.; Deng, Q. Enhancing surface polarization and reducing bandgap of $BaTiO_3$ nanofiller for preparing dielectric traits-improved composites via its hybridization with layered g-C_3N_4. *Surf. Interfaces* 2022, *31*, 102060.

55. Peng, W.; He, X.; Li, J.; Chen, X.; Chen, Z.; Huang, G. Photocatalytic removal and mechanistic investigation of U(VI) using $BaTiO_3$/g-C_3N_4 heterojunctions with enhanced efficiency. *Environ. Res.* 2026, 303(1), 124551. https://doi.org/10.1016/j.envres.2026.124551

56. McCreary, K.M.; Hanbicki, A.T.; Sivaram, S.V.; Jonker, B.T. A- and B-exciton photoluminescence intensity ratio as a measure of sample quality for transition metal dichalcogenide monolayers. *APL Mater.* 2018, 6, 111106. https://doi.org/10.1063/1.5053699

57. Ning, X.; Meng, S.; Fu, X.; Ye, X.; Chen, S. Efficient utilization of photogenerated electrons and holes for photocatalytic selective organic syntheses in one reaction system using a narrow band gap CdS photocatalyst. *Green Chem.* 2016, *18*, 3628–3639.

58. Mahesh, A.; Jawahar, I.; Biju, V. Photoluminescence, photocurrent response and photocatalytic activity of hydrothermally derived nanocrystalline ZnO with native point defects. *J. Cryst. Growth* 2024, *648*, 127894.

59. Liu, H.; Wu, Z.; Shao, J.; Yao, D.; Gao, H.; Liu, Y.; Yu, W.; Zhang, H.; Yang, B. $CsPb_xMn_{1-x}Cl_3$ perovskite quantum dots with high Mn substitution ratio. *ACS Nano* 2017, *11*, 2239–2247.

60. Katoh, R.; Takahashi, K.; Sugawa, K. Quantum yields of photoluminescence of TiO_2 photocatalysts. *J. Phys. Chem. C* 2022, *126*, 20954–20959.

61. Kalidasan, K.; Mallapur, S.; Kumar, S.G. Pivotal role of surface and bulk Gd species in WO_3 to promote Type-II charge carrier transfer pathways in Gd-WO_3/g-C_3N_4 heterojunction photocatalyst. *J. Environ. Chem. Eng.* 2024, *12*, 113054.

62. Molla, M.A.I.; Furukawa, M.; Tateishi, I.; Katsumata, H.; Suzuki, T.; Kaneco, S. Photocatalytic decolorization of dye with self-dye-sensitization under fluorescent light irradiation. *ChemEngineering* 2017, *1*, 8.

63. Anisuzzaman, S.; Joseph, C.G.; Pang, C.K.; Affandi, N.A.; Maruja, S.N.; Vijayan, V. Current trends in the utilization of photolysis and photocatalysis treatment processes for the remediation of dye wastewater: A short review. *ChemEngineering* 2022, *6*, 58.

64. Tran, H.D.; Nguyen, D.Q.; Do, P.T.; Tran, U.N. Kinetics of photocatalytic degradation of organic compounds: A mini-review and new approach. *RSC Adv.* 2023, *13*, 16915–16925.

65. Alqarni, L.S.; Goda, M.N.; Albadri, A.; Taha, K.K.; Alharbi, A.A.; Ismail, M.; Modwi, A. Improved photodegradation of indigo carmine dye (IC) via chromium-TiO_2@g-C_3N_4 heterojunctions. *Diamond Relat. Mater.* 2025, 113055.

66. Alqarni, L.S.; Goda, M.N.; Albadri, A.; Ismail, M.; Taha, K.K.; Modwi, A. Photocatalytic decomposition of organic dyes via κ-Al_2O_3@Cr_2O_3 loaded on g-C_3N_4 nanostructures. *J. Mater. Sci. Mater. Electron.* 2025, *36*, 1625.

67. Arslan, H.; Eskikaya, O.; Bilici, Z.; Dizge, N.; Balakrishnan, D. Comparison of Cr(VI) adsorption and photocatalytic reduction efficiency using leonardite powder. *Chemosphere* 2022, *300*, 134492.

68. Qudsieh, I.Y.; Ali, M.A.; Maafa, I.M. Effect of water matrix on photocatalytic degradation of organic pollutants in water: A literature review. *Rev. Chem. Eng.* 2025, *41*, 539–573.

69. Goutomo, B.T.; Ouzar, A.; Kim, I.-K. Optimized decolorization of aniline blue dye using potassium ferrate(VI). *Desalin. Water Treat.* 2025, *321*, 101006.

70. Meena, S.; Sethi, M.; Saini, S.; Kumar, K.; Saini, P.; Meena, S.; Kashyap, S.; Yadav, M.; Meena, M.L.; Dandia, A. Molecular surface-dependent light harvesting and photo charge separation in plant-derived carbon quantum dots for visible-light-driven OH radical generation for remediation of aromatic hydrocarbon pollutants and real wastewater. *J. Colloid Interface Sci.* 2024, *660*, 756–770.

71. Alnafisah, A.S.; Khezami, L.; Hamadi, N.B.; Modwi, A.; Alsulami, A.; Taha, K.K. Enhanced visible-light photodegradation of Congo red using ultrasonication-prepared $LaCoO_3$@g-C_3N_4 nanocomposites. *Diam. Relat. Mater.* 2025, *157*, 112491.

72. Liu, J.; Han, X.; Zhang, T.; Tian, K.; Li, Z.; Luo, F. Reactive oxygen species (ROS) scavenging biomaterials for anti-inflammatory diseases: From mechanism to therapy. *J. Hematol. Oncol.* 2023, *16*, 116.

73. Menon, K.; Lopis, A.D.; Choudhari, K.; Kulkarni, B.; Maradur, S.; Kulkarni, S.D. Scavenger-free solar photocatalytic degradation of textile dyes and antibiotics using magnetically separable bi-junctional photocatalyst. *Mater. Res. Bull.* 2025, *181*, 113074.

74. Nosaka, Y.; Nosaka, A. Understanding hydroxyl radical (•OH) generation processes in photocatalysis. *ACS Energy Lett.* 2016, *1*, 356–359.

75. Ashouri, R.; Rasekh, B.; Kasaeian, A.; Sheikhpour, M.; Yazdian, F.; Dehghani Mobarakeh, M. Effect of ZnO-based nanophotocatalyst on degradation of aniline. *J. Mol. Model.* 2021, *27*, 92.

76. Thakurata, D.G.; Das, K.C.; Dhar, S.S. Efficient photocatalytic degradation of aniline blue under solar irradiation by ternary cobalt ferrite/graphitic carbon nitride/bentonite nanocomposite. *Environ Sci Pollut Res* 2022, 29, 34269–34277. https://doi.org/10.1007/s11356-021-18242-3

77. Azzam, A.B.; El-Sheikh, S.; Geioushy, R.; Salah, B.A.; El-Dars, F.M.; Helal, A.S. Facile fabrication of a novel $BiPO_4$ phase junction with enhanced photocatalytic performance towards aniline blue degradation. *RSC Adv.* 2019, *9*, 17246–17253.

78. Vásquez, D.; Palominos, F.; Martínez, S. Visible-light photocatalytic degradation of aniline blue by stainless-steel foam coated with TiO_2 grafted with anthocyanins from a maqui-blackberry system. *Catalysts* 2020, *10*, 1245.

79. Egzar, H.K.; Mashkour, M.S.; Juda, A.M. Study the photodegradation of aniline blue dye in aqueous phase by using different photocatalysts. *Asian Trans. Basic Appl. Sci.* 2013, *3*, 23–28.

80. Ong, W.-J.; Tan, L.-L.; Ng, Y.H.; Yong, S.-T.; Chai, S.-P. Graphitic carbon nitride ($g\text{-}C_3N_4$)-based photocatalysts for artificial photosynthesis and environmental remediation: Are we a step closer to achieving sustainability? *Chem. Rev.* 2016, *116*, 7159–7329.

81. Zhang, N.; Ciriminna, R.; Pagliaro, M.; Xu, Y.-J. Nanochemistry-derived Bi_2WO_6 nanostructures: Towards production of sustainable chemicals and fuels induced by visible light. *Chem. Soc. Rev.* 2014, *43*, 5276–5287.

82. Kumar, S.; Baruah, A.; Tonda, S.; Kumar, B.; Shanker, V.; Sreedhar, B. Cost-effective and eco-friendly synthesis of novel and stable N-doped $ZnO/g\text{-}C_3N_4$ core–shell nanoplates with excellent visible-light responsive photocatalysis. *Nanoscale* 2014, *6*, 4830–4842.

83. Dong, F.; Zhao, Z.; Xiong, T.; Ni, Z.; Zhang, W.; Sun, Y.; Ho, W.-K. In situ construction of $g\text{-}C_3N_4/g\text{-}C_3N_4$ metal-free heterojunction for enhanced visible-light photocatalysis. *ACS Appl. Mater. Interfaces* 2013, *5*, 11392–11401.

84. Wang, J.; Tang, L.; Zeng, G.; Deng, Y.; Liu, Y.; Wang, L.; Zhou, Y.; Guo, Z.; Wang, J.; Zhang, C. Atomic scale $g\text{-}C_3N_4/Bi_2WO_6$ 2D/2D heterojunction with enhanced photocatalytic degradation of ibuprofen under visible light irradiation. *Appl. Catal. B Environ.* 2017, *209*, 285–294.

85. Perween, S.; Ries, K.M.; Hofmann, A.; Aalto, T.H.; Fernández, H.M.; Widenmeyer, M.; Löser, R.; Timm, J.; Schmitz, G.; Atanasova, P. Structural origins of photocatalytic properties in Ruddlesden–Popper $Sr_{n+1}Ti_nO_{3n+1}$ (n = 1, 2) and their topochemically fluorinated phases $Sr_{n+1}Ti_nO_{(3n+1)-x}F_{2x}$ (x ≈ n). *J. Mater. Chem. A* 2026, *14*, 15119–15141.

86. Yuan, Y.; Guo, R.-T.; Hong, L.-F.; Ji, X.-Y.; Lin, Z.-D.; Li, Z.-S.; Pan, W.-G. A review of metal oxide-based Z-scheme heterojunction photocatalysts: Actualities and developments. *Mater. Today Energy* 2021, *21*, 100829.

87. Talukdar, S.; Dutta, R.K. A mechanistic approach for superoxide radicals and singlet oxygen mediated enhanced photocatalytic dye degradation by selenium doped ZnS nanoparticles. *RSC Adv.* 2016, *6*, 928–936.

88. Murali, R.; Amirthavalli, C. Defect assisted reactive oxygen species generation for photocatalytic degradation of methylene blue by nano-structured zinc oxide synthesized in CTAB medium. *Mater. Chem. Phys.* 2023, *294*, 127014.

89. Alam, U.; Pandey, K.; Verma, N. Photocatalytic oxidation of glyphosate and reduction of Cr(VI) in water over ACF-supported $CoNiWO_4$-gCN composite under batch and flow conditions. *Chemosphere* 2022, *297*, 134119.

90. Pandey, A.; Gupta, A.; Alam, U.; Verma, N. Construction of a stable S-scheme $NiSnO_3$/g-C_3N_4 heterojunction on activated carbon fibre for the degradation of glyphosate in water under flow condition. *Chemosphere* 2024, *347*, 140709.

91. Usman, M.; Zeb, Z.; Ullah, H.; Suliman, M.H.; Humayun, M.; Ullah, L.; Shah, S.N.A.; Ahmed, U.; Saeed, M. A review of metal-organic frameworks/graphitic carbon nitride composites for solar-driven green H_2 production, CO_2 reduction, and water purification. *J. Environ. Chem. Eng.* 2022, *10*, 107548.

92. Chen, D.; Cheng, Y.; Zhou, N.; Chen, P.; Wang, Y.; Li, K.; Huo, S.; Cheng, P.; Peng, P.; Zhang, R. Photocatalytic degradation of organic pollutants using TiO_2-based photocatalysts: A review. *J. Clean. Prod.* 2020, *268*, 121725.

93. Hossain, M.S.; Mollah, M.Y.A.; Susan, M.A.B.H.; Islam, M.M. Role of in situ electrogenerated reactive oxygen species towards degradation of organic dye in aqueous solution. *Electrochim. Acta* 2020, *344*, 136146.

94. Edge, R.; Truscott, T.G. The reactive oxygen species singlet oxygen, hydroxy radicals, and the superoxide radical anion—Examples of their roles in biology and medicine. *Oxygen* 2021, *1*, 77–95.

95. Du, J.; Wang, C.; Zhao, Z.; Cui, F.; Ou, Q.; Liu, J. Role of oxygen and superoxide radicals in promoting H_2O_2 production during VUV/UV radiation of water. *Chem. Eng. Sci.* 2021, *241*, 116683